



OPEN Study on mechanical properties of rock like samples with prefabricated holes under specific temperatures

Cheng Lu-ping¹, Xiong Zu-qiang¹, Ji Xue-long¹ & Wang Chun^{1,2}✉

Based on the volume shrinkage characteristics of expandable polystyrene (EPS) particles after heating, holes were randomly constructed in the interior of rock-like samples containing EPS particles after heating. The axial compression test was carried out on the rock-like samples, and then the failure process of samples with prefabricated holes under uniaxial compression was simulated by the particle flow software PFC2D. Therefore, the influences of diameter and porosity of precast holes on the mechanical properties, crack evolution and failure characteristics of rock-like samples were explored. The results show that the pore-forming effect in specimen was most evident under the heating of 200 °C, which has a relatively small impact on the strength of the sample. The larger the pore diameter and porosity inside the sample, the lower the peak stress and the larger the peak strain, and even the strain mutation could appear. Moreover, the development of internal cracks in the sample is closely related to the pore diameter and porosity according to the results of PFC2D simulation. Furthermore, cracks generate firstly at the pore locations and then expand to the area surrounding the holes, and form a through crack ultimately. Besides, both tensile stress and shear stress play a significant role during the uniaxial compression failure process of the sample with pores, indicating that failure is not solely due to tensile stress. Although there are slight deviations between the stress-strain curves of indoor tests and numerical simulations, the overall trends are basically consistent.

Keywords Prefabricated holes, PFC2D, Mechanical properties, Crack development, Failure characteristics

After being subjected to complex geological structure, natural reservoir rocks develop undoubtedly internal defects such as holes, fractures and joints. These existing internal defects directly affect the physical and mechanical properties of rocks, and they are likely to lead to the instability and failure of the rock mass. Additionally, the interaction among different types of internal defects has a significant impact on the mechanical properties and failure modes of the rock mass. For instance, the quantity, size, shape and distribution of holes could influence the mechanical characteristics and damage evolution laws of the rock mass^{1–5}. Therefore, in-depth research on the mechanical properties, crack propagation and failure characteristics of rocks with holes under loading is of great significance for solving the stability of underground engineering rock mass^{6,7,8}.

Natural rock masses exhibit a complex and disordered spatial distribution of primary defects. To address this significance, scholars at home and abroad have carried out in-depth studies on the complex spatial distribution of primary defects in natural rock masses and their impacts. For example, the complex evolution process of crack propagation and fracture mode in fractured rocks were explored by researchers through prefabricating cracks on rock samples^{9–11}. Besides, DAI Bing et al.¹² and WANG Yanbing et al.¹³ explored the dynamic characteristics, damage characteristics, and energy evolution law of hole-containing rocks under impact loads. Based on acoustic emission tests, PEI Xiangjun et al.¹⁴, ZHENG Lei et al.¹⁵ and ZHOU Yu et al.¹⁶ revealed the acoustic emission characteristic parameters of defective rocks in different cracking stages—findings that provide a theoretical basis for the failure mechanism of rock masses. Meanwhile, the influence of pre-fracture orientation on the structural characteristics and fracture modes of rock samples under increasing fatigue loading was researched by WANG Yu et al.¹⁷, indicating that a larger fracture angle makes the rock less prone to fatigue failure. WU Tianhua et al.¹⁸, ZHAO Guoyan et al.¹⁹, MA Bin et al.²⁰ and LI Yangyang et al.²¹ conducted uniaxial compression tests on porous rocks to investigate the peak strength, deformation, failure characteristics, and the incubation and evolution

¹School of Energy Science and Engineering, Henan Polytechnic University, Jiaozuo 454003, China. ²Collaborative Innovation Center of Coal Work Safety and Clean High Efficiency Utilization, Henan Polytechnic University, Jiaozuo 454003, Henan, China. ✉email: wangchun@hpu.edu.cn

SiO ₂	Al ₂ O ₃	CaO	MgO	Fe ₂ O ₃	Others
20.6%	5.0%	62.3%	3.6%	3.5%	5.0%

Table 1. Components of composite portland cement.

Sieve size/mm	Retention mass/%	Accumulated retention mass/%
1.35	0.00	0.00
1.00	2.64	2.64
0.60	94.00	96.64
0.45	1.40	98.04
less than 0.30	1.96	100.00

Table 2. The size distribution of quartz sand after sieving.

laws of cracks in the specimens. In addition to the uniaxial compression test, LI Zhengyi et al.²² and ZHANG Baoliang et al.²³ analyzed the damage evolution law of hole-containing rocks and its influence on mechanical properties (e.g., strength and deformation) based on triaxial tests. Moreover, SI Yujie et al.²⁴ studied the failure characteristics of a triaxial compression particle model containing co planar double fractured composite rocks under different confining pressures, fracture angles, and fracture lengths, and found that the failure mode of the rock sample was mainly controlled by the fracture angle. It was also demonstrated that the holes in rocks weaken rock strength significantly via the FDEM numerical simulation method, and square and circular holes exhibit less weakening effect when compared to other investigated hole shapes²⁵. Additionally, FAN Xingyu et al.²⁶, ZHANG Xuepeng et al.²⁷, LI Chongjin et al.²⁸ and SUN Jielong et al.²⁹ simulated the failure process of defective rock samples under uniaxial or biaxial compression via the PFC2D numerical simulation software, and elaborated on the law of crack initiation and evolution during the load-induced damage of the samples.

In summary, current research on defective rocks mainly focuses on regularized and simplified defect morphologies, such as regularly arranged fractures, a small number of pores with fixed shapes and positions, and specific combinations of these defects, ignoring the randomness of internal defect in natural rocks. Furthermore, most studies have concentrated on fractures and holes that penetrate the rock mass or extend from the rock surface to the interior. However, the experimental method of randomly constructing holes inside the specimen by heating EPS particles remains relatively underutilized in existing research. To address this research gap, this study heated rock-like specimens containing EPS particles to randomly generate spherical holes within them. Compared with the regular defects used in previous studies, this approach effectively compensates for the prior oversight of the actual occurrence states of irregular spatial positions and pore sizes of defects in natural rocks. On this basis, axial compression tests and the PFC2D numerical simulation technology were combined to explore systematically the influence of the two key parameters (pore size and porosity) on the mechanical properties and failure modes of rocks.

Test scheme

Material preparation

The composite Portland cement with compressive strength of 42.5MPa was selected in the test. It was made by grinding Portland cement clinker, appropriate amount of gypsum and more than two kinds of mixed materials, and the chemical composition was shown in Table 1.

Quartz sand is a kind of quartz particle formed by crushing and grinding of quartz stone, and its main chemical composition is SiO₂. The particle size distribution of quartz sand used in the test is shown in Table 2.

EPS foam particles are formed by softening polystyrene resin with a foaming agent, and they have good water absorption, light weight and significant volume shrinkage when heated. Therefore, EPS foam particles with different particle sizes were added to the rock-like sample, and holes were randomly formed in the sample after heating. EPS foam particles with particle sizes of 1 mm, 2 mm, 3 mm, 4 mm and 5 mm were selected for the test, as shown in Fig. 1.

To explore the appropriate heating temperature for pore formation, four temperature gradients of 100 °C, 200 °C, 300 °C and 400 °C were set. The prepared samples were placed in a muffle furnace and heated to the specified temperature and held for 4 hours. After the samples cooled naturally, they were cut and the shrinkage of the EPS particles and the pore formation effect were observed carefully. Fig. 2 shows the longitudinal section of the heated samples containing 5 mm EPS particles under different temperatures.

From Fig. 2, it can be observed that the volumes of EPS particles were almost completely reduced when the heating temperature reached 200 °C or higher, resulting in a significant pore-forming effect. Considering that excessively high temperatures may cause damage to the samples, the final heating temperature was set at 200 °C, with a heating rate of 5 °C/min and a holding time of 4 hours. Subsequently, samples containing EPS particles of different particle sizes were subjected to the same heating treatment. After cutting, the internal pore formation was examined, as shown in Fig. 3. It was found that samples with EPS particles of varying sizes exhibited good pore-forming effects.

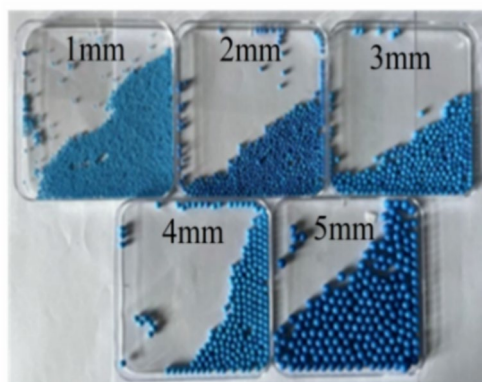


Fig. 1. Physical drawing of EPS foam particles with five particle sizes.

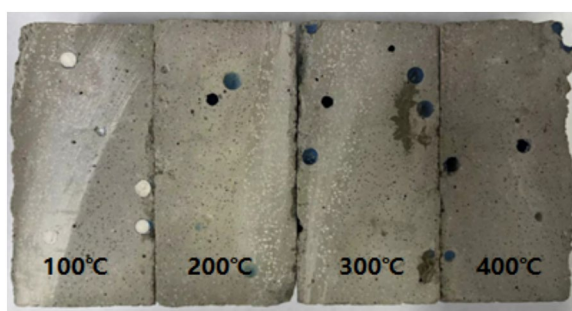


Fig. 2. Sectional view of the specimens under four different heating temperatures (5mm).

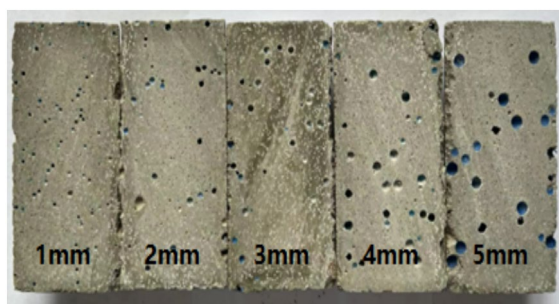


Fig. 3. Sectional views of the specimens with different pore sizes formed after heating.

Cement	Quartz sand	Water	Water-reducing admixture	Defoamer
100%	35%	40%	1%	1%

Table 3. Mass ratio of each component in specimen.

Specimen preparation

Cement, quartz sand and admixtures were selected as raw materials to prepare standard cylindrical specimens with a diameter of 50 mm and a height of 100 mm. The mass proportions of each component are listed in Table 3. Both ends of the specimens were carefully polished to ensure that their surface roughness, flatness, and verticality met the requirements for rock mechanics testing.

As shown in Table 3, the raw materials were weighed using an electronic scale and added to water in several portions while continuously stirring until uniformly mixed. Then, pre-sorted EPS particles were added to the corresponding mixtures. After thorough mixing, the mixture was poured into standard cylindrical molds and demolded after being left at room temperature for 24 hours. The demolded specimens were tightly wrapped with

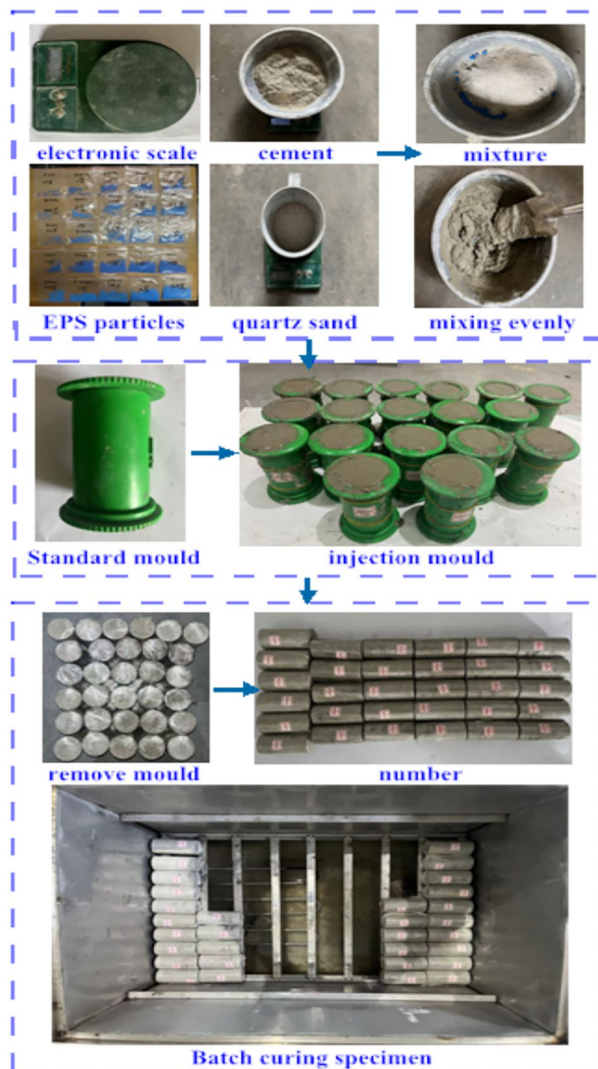


Fig. 4. Preparation process of specimens.

EPS particle size/mm	design porosity/%	heating temperature/°C
1	0.5	200
2	1.0	
3	1.5	
4	2.0	
5	2.5	

Table 4. Design scheme of orthogonal test.

plastic film and placed in a curing box for full hydration. The curing temperature was maintained at 20°C, and the curing period was 7 days. The specimen preparation process is illustrated in Fig. 4.

Test design

The pore size and porosity of the specimens were controlled by incorporating EPS particles of different sizes and quantities into the raw material mixtures. Based on an orthogonal design scheme, both the particle size and porosity of the EPS particles were considered variable factors. Each particle size corresponded to specimen porosities of 0.5%, 1%, 1.5%, 2%, and 2.5%, respectively, as detailed in Table 4.

Moreover, to minimize the impact of experimental errors or invalid specimens on the results, three specimens were prepared for each single variable factor. In total, 75 specimens containing EPS particles were fabricated. Additionally, six non-porous specimens were prepared for comparative analysis of strengthened before and after heating, with three specimens heated to 200°C and the other three left unheated.

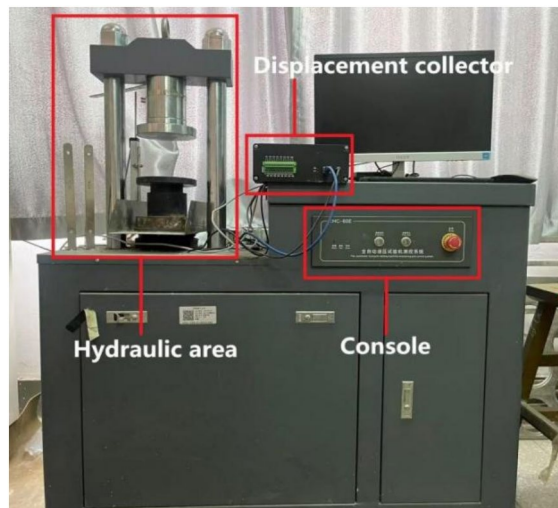


Fig. 5. The test equipment.

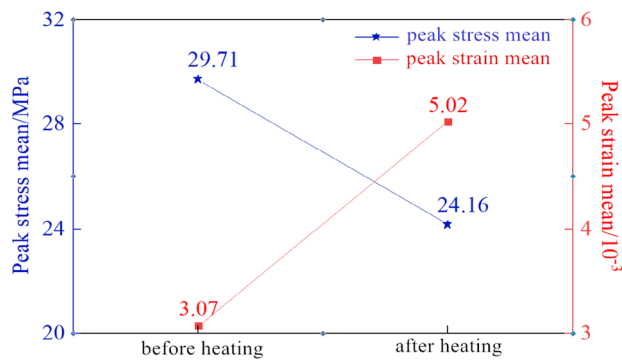


Fig. 6. The mean values of peak stress and peak strain of non-porous specimens before or after heating.

According to the test scheme, the cured specimens were placed into a muffle furnace. The heating rate was precisely controlled at $5^{\circ}\text{C}/\text{min}$, which was increasing from ambient temperature to 200°C , followed by a 4-hour holding period to ensure complete thermal shrinkage of the EPS particles and optimal pore formation. After heating, the specimens were removed once the furnace had cooled naturally to room temperature, and their physical properties were measured. Thereafter, uniaxial compressive strength tests were conducted using a fully automatic YWA-150B hydraulic testing machine under displacement-controlled loading at a rate of 0.02 mm/s . During the loading process, the MLT16-SDAQ high-precision displacement acquisition instrument was used simultaneously to record the displacement data of the specimen under compression. Meanwhile, a high-speed camera, with the assistance of an LED fill light, captured synchronously the relevant image information, providing preparation for subsequent analysis. The testing equipment is presented in Fig. 5.

Test results

Stress and strain analysis of non-porous specimen

Since appearance changes can reflect the types of thermal-induced damage and provide a physical damage basis for the subsequent analysis of the influence of thermal effects on the mechanical properties of the specimen, the changes in the appearance and weight of the non-porous specimens before and after heating were compared. The mass of the non-porous specimens showed a significant decrease before and after heating: The average mass was 385 g before heating, which decreased to 330 g after heating, primarily due to the evaporation of internal moisture under high temperatures. Additionally, the surface color of the specimens lightened, and their texture became powdery. Small cracks appeared on the specimens' surfaces, which were caused by the different expansion coefficients of quartz sand and cement during the heating process, leading to uncoordinated deformation between the two. Furthermore, some specimens exhibited surface detachment and pores, with the pores in these areas predominantly showing regular spherical shapes. This phenomenon can be attributed to gas generation from EPS particles on the specimens' surfaces during heating, causing internal expansion and subsequent partial material detachment. Uniaxial compression tests conducted on six non-porous specimens yielded the mean values of peak stress and peak strain, as illustrated in Fig. 6.

As shown in Fig. 6, the mean peak stress of the non-porous specimens before heating treatment reached 29.71 MPa, while it decreased to 24.16 MPa after heating treatment, indicating a slight reduction in mechanical strength. In contrast, the mean peak strain increased significantly after heating treatment. This discrepancy may be attributed to the differential thermal expansion behaviors of the specimens' constituent materials, which could lead to the formation of micro-cracks and exacerbated internal damage. Moreover, the evaporation of capillary water within the specimens likely facilitated the formation of more coherent fluid transmission channels. As tiny pores gradually interconnected and expanded, the internal structure sustained progressively severe damage. Consequently, the specimens exhibited characteristics of reduced strength and increased deformation.

Stress and strain analysis of specimen with holes

By analyzing the stress-strain curves of the specimens, the influence of pore size and porosity on mechanical properties was investigated. Figs. 7(a) and 7(b) present the stress-strain curves of specimens with identical void diameters but varying porosities under uniaxial compression. Specifically, Fig. 7(a) displays the curves for specimens with an internal pore diameter of 3 mm and porosities ranging from 0.5% to 2.5%. Similarly, Fig. 7(b) shows the stress-strain curves when the internal void diameter is 4 mm and the porosity ranges from 0.5% to 2.5%.

In Fig. 7(a), as porosity increased from 0.5% to 2.5%, the peak stress decreased from 21.0 MPa to 11.1 MPa, representing a reduction of 46.5%. This trend indicates that higher porosity correlates with lower peak stress and diminished load-bearing capacity. The underlying reason is that increased porosity corresponds to a larger internal pore volume, thereby reducing the effective load-bearing area of the solid skeleton. Under the same external load, this results in higher stress per unit area, making the specimen more susceptible to reaching its strength limit. Additionally, stress concentration occurs around the pores, creating weak zones that are prone to initiate and propagate micro-cracks at relatively low stress levels. Higher porosity intensifies this stress concentration, further decreasing the peak stress. Conversely, as the porosity increases from 0.5% to 2.5%, the relative increase in peak strain exceeds 130%, which thereby indicates a significant enhancement in deformation capacity. This increase can be explained by the compressibility of pores under axial pressure; greater porosity implies a larger volume of compressible pores, allowing for more accommodated deformation. Consequently, specimens with higher porosity exhibit greater strain and are more likely to develop micro-cracks under the same axial load. These micro-cracks progressively expand and connect under continued loading, resulting in increased deformation and intensified internal damage.

In Fig. 7(b), when the porosity is 2.5% and the stress approaches 10 MPa, a nearly horizontal section appears on the stress-strain curve, that is, the strain increases rapidly when the stress increases slightly. Further analysis reveals that pore diameter and porosity are the key parameters regulating this strain mutation phenomenon. On one hand, large pore diameters increase the stress concentration coefficient at pore edges, providing "initial

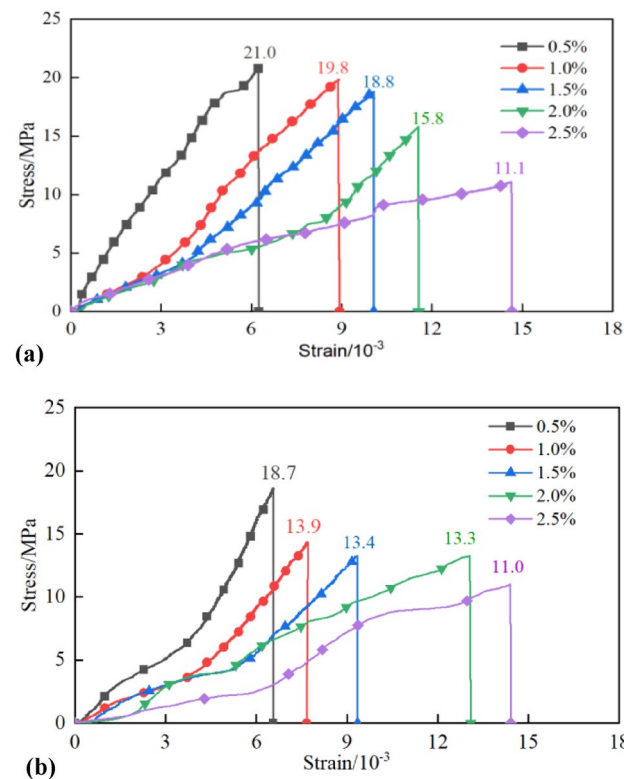


Fig. 7. (a) The stress-strain curves with 3 mm pore size (0.5%~2.5% porosity). (b) The stress-strain curves with 4 mm pore size (0.5%~2.5% porosity).

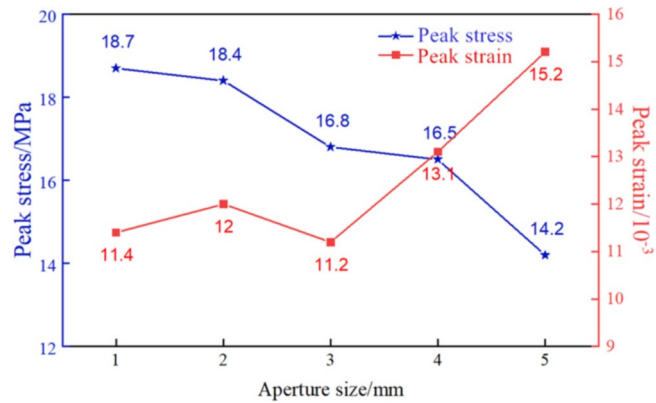


Fig. 8. The curves of peak stress and peak strain of different pore sizes (1.5% porosity).

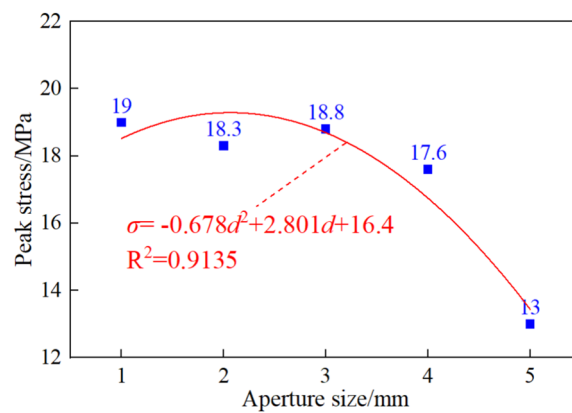


Fig. 9. Fitting diagram of peak stress mean of specimen (1.5% porosity).

damage sources" for strain mutation. Specifically, the larger the pore diameter, the smaller the relative distance between pores and specimen boundaries; this weakens the "stress dispersion effect" of boundary constraints on pore edge stress, while the stress gradient at pore interfaces becomes more concentrated. As a result, microcracks propagate along the direction of maximum stress, preventing random deflection of cracks caused by small pore diameters and laying the foundation for subsequent rapid penetration. On the other hand, high porosity reduces pore spacing and increases the probability of crack connection, shifting microcracks from "dispersed initiation" to "explosive penetration" and triggering strain mutation ultimately.

To investigate the effect of pore size on the peak stress and peak strain of specimens with identical porosity, uniaxial compression test results for specimens with a fixed porosity of 1.5% and pore diameters ranging from 1 mm to 5 mm were analyzed. Fig. 8 shows the axial peak stress and strain curves of samples with different pore sizes at a porosity of 1.5%.

As shown in Fig. 8, at a porosity of 1.5%, the peak stress of the specimens decreases with increasing pore diameter. This is because a larger pore diameter leads to more pronounced stress concentration around pores. And these stress-concentrated regions first generate, propagate, and penetrate microcracks under axial pressure, which can reduce the peak stress that the rock can withstand. Furthermore, the peak strain increases generally with increasing pore diameter. It indicates that larger pore sizes make the internal structure of rocks looser, similar to forming some compressible "spaces" in specimens. Therefore, the pores are more prone to inward compressive deformation under axial pressure, which in turn leads to an increase in peak strain. However, when the pore diameter ranges from 1 to 3 mm, the peak strain shows no obvious increasing trend. This indicates that the sparse degree of pore distribution is moderate in this pore diameter range, and it neither causes "stress congestion" due to dense pores nor leads to "stress overload" due to excessively large pores. So the uniformity of stress transmission enables coordinated deformation of the rock as a whole, thus resulting in no significant fluctuation in peak strain.

To further explore the relationship between peak stress and internal pore size, a fitting analysis is conducted on the mean values of peak stress of specimens at a porosity of 1.5%, as shown in Fig. 9. The data indicate an overall decreasing trend in mean values of peak stress with increasing pore diameter. Notably, when the pore size increases from 3 mm to 5 mm, the rate of decrease in mean values of peak stress becomes significantly steeper. This behavior reflects the nonlinear intensification of the stress concentration effect: larger pores require

lower critical stress to initiate crack propagation. Therefore, specimens with large-aperture holes quickly reach the crack propagation conditions at the initial stage of loading, and the cracks rapidly expand along the edge of the large holes to form the main crack, resulting in a sudden drop in the overall load-bearing capacity of the specimen.

Analysis of failure characteristics

It is generally accepted that the failure characteristics of porous specimens are the external manifestations of their internal mechanical properties, which can reflect the mechanical characteristics of the specimen to some extent. Fig. 10 presents the failure modes of specimens with a pore size of 3 mm and varying porosities (0%~2.5%) after undergoing uniaxial compression tests.

As illustrated in Fig. 10, specimens with porosities of 0% and 0.5% contain few internal defects. Under uniaxial compression, vertical through-cracks perpendicular to the loading direction tend to form, resulting in tensile failure. After failure, the specimen remains relatively intact, typically breaking into elongated fragments. When the porosity exceeds 1.0%, multiple cracks originate from one end of the specimen. The stress state at the crack tip slowly changes from tensile dominance to shear dominance, inducing more secondary shear cracks. Finally, the specimens break into larger wedge-shaped fragments and powder-like debris. At this point, the integrity of the specimen is poor, and a composite failure mode of “tension-shear” is formed ultimately. Moreover, higher porosity leads to more powdery debris after damage. This occurs because, at low porosity levels, the distance between pores is large, and interactions among them are minimal, allowing for the formation of a single dominant crack similar to non-porous specimens. However, as porosity increases, tensile failure may still occur at the top and bottom ends of the pores, while conjugate shear cracks develop in the rock bridges between adjacent pores due to stress concentration. These shear cracks are prone to connect and propagate, shifting the failure mechanism from pure tension to a combination of tension and shear. As inherent weak zones, pores are more susceptible to cracking and collapse under compression. When cracks around multiple pores link together, dense pore-related defects appear on the fracture surface. Concurrently, the increase in powdered debris suggests intensified internal friction during the compression process.

Numerical simulation of PFC2D

Model establishment and parameters calibration

The basic unit of the PFC2D numerical simulation software consists of spherical particles, which interact with each other through contact forces. During the simulation of compression tests, it is necessary to define boundary walls at the upper and lower surfaces of the model. By applying displacement control to these walls, uniaxial compression of the specimen can be effectively achieved.

Given that the experimental material resembles rock-like materials, a parallel bonding model was employed to better capture their elastic-plastic mechanical behavior. This model treats the bonded material as a series of springs arranged in parallel, possessing constant normal and tangential stiffness, capable of transmitting both force and torque simultaneously, and the working principle of the parallel bonding model is shown in Fig. 11. With the macroscopic mechanical indices of laboratory uniaxial compression tests, the methods of “trial-and-error method” and “sensitivity analysis” in PFC2D simulations are used to calibrate the mesoscopic parameters of the model, and the results presented in Table 5.

The specimen model has a width of 5 cm and a height of 10 cm, containing approximately 8,500 to 9,300 particles. The radius of cement particles ranges from 0.02 mm to 0.03 mm, whereas those of quartz sand particles vary between 0.03 mm and 0.05 mm. The dimensions, particle composition, and bonding configuration of the model are depicted in Fig. 12.

According to the indoor test results, EPS particles were randomly generated in the model to build the model of the specimens with holes, and then the generated EPS particles were removed to obtain the model with non-

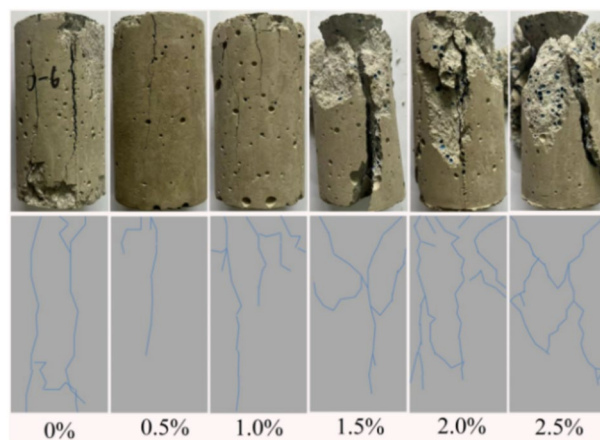


Fig. 10. Failure Characteristics of specimens with pore size of 3 mm (0%~2.5% porosities).

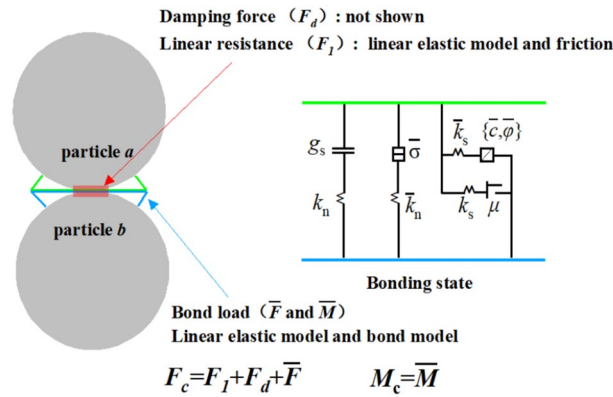


Fig. 11. The operating principle of parallel bonding mode. Note: In Fig. 11, F_c , F_l and \bar{F} are the resultant force, linear contact force and parallel bonding force respectively. M_c and \bar{M} represent the contact moment and the parallel bonding moment respectively. g_s is the surface gap, which indicates the difference between the actual distance between particles and the sum of their radii. When $g_s < 0$, it means the particles are in contact; otherwise, they are separated. k_n and k_s are the normal stiffness and tangential stiffness respectively, and μ is the friction coefficient. \bar{c} , $\bar{\sigma}$ and $\bar{\varphi}$ represent the cohesion, tensile strength and friction angle of the parallel bond model respectively. After the contact failure of the parallel bonding model, the contact model between particles changes from the parallel bonding model to the linear contact model.

Medium	Maximum particle radius/mm	Minimum particle radius/mm	Particle density/ $g \cdot cm^{-3}$	Particle contact modulus/GPa	Particle stiffness ratio	Friction coefficient μ	Parallel bond modulus/GPa	Normal stiffness k_s /MPa	Tangential stiffness k_n /MPa
Cement	0.03	0.02	3.1	10	0.8	0.45	1.5	23	27
Quartz sand	0.05	0.03	2.3	13	1.4	0.5	1.0	20	24
EPS	5	1	0.2	1	0.03	0.45	0.1	0.5	0.5

Table 5. Microscopic parameters of numerical simulation. Note: The mesoscale parameters in the table were calibrated by laboratory test, and the peak stress (23.8 MPa) and elastic modulus (3.5 GPa) of the non-porous specimen were taken as the target indexes.

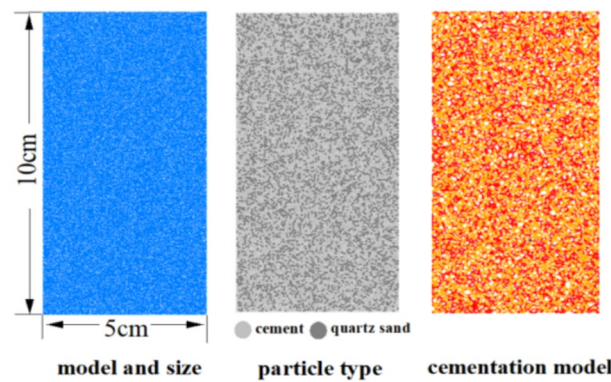


Fig. 12. The 2D Model of the specimen.

uniform holes. The model diagram with a porosity of 2.5% and a pole diameter ranges from 1 mm to 5 mm is shown in Fig. 13. The blue dots represent the EPS particles, which are displayed as white dots after removal.

Damage characteristics and cracks propagation

Based on laboratory test, the PFC2D software was used to simulate uniaxial loading tests of specimens with internal holes, so the influence of the pole diameter and porosity on the crack evolution of the specimens was further analyzed. Additionally, to correspond with the indoor test, displacement loading method was used for simulation, with a loading rate of 0.02mm/s. When the porosity was 2.5%, the failure diagrams with different pole diameters inside the specimens are shown in Fig. 14.

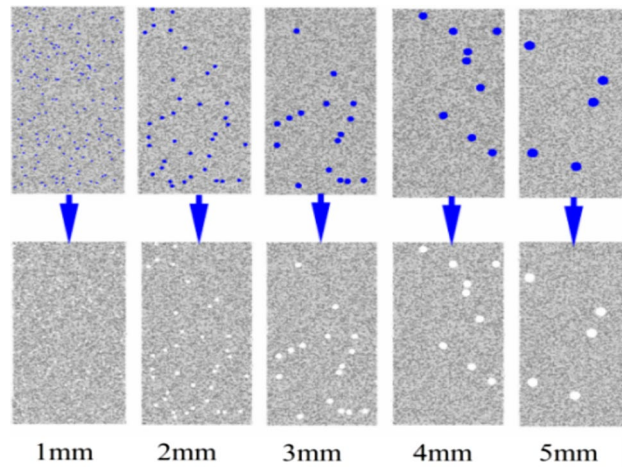


Fig. 13. Models of specimens with different pore sizes (2.5% porosity).

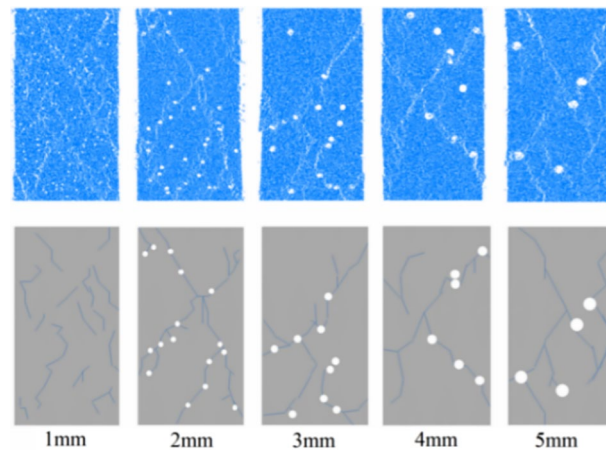


Fig. 14. Failure Modes of specimens with different pore sizes (2.5% porosity).

In Fig. 14, the damaged model has small cracks inside the specimens and no obvious macroscopic cracks that penetrate when the pore diameter is 1 mm, indicating good integrity of specimens after damage. However, when the pore diameter is 2 mm, obvious penetrating cracks are observed in the damaged model. As the pore diameter increases further, the model not only exhibits more extensive penetrating cracks, but also shows peeling or sliding at the crack edges. These phenomena ultimately lead to the specimen being split into several segments by the propagating cracks. By observing the crack location, it is found that the cracks are related closely to the position of the internal holes. Multiple internal holes are connected along the path of the penetrating crack, and the paths between some holes almost overlap with the penetrating crack. Meanwhile, most of the holes along the crack path have undergone significant deformation. Additionally, the non-penetrating cracks inside the model are often terminated by holes and connected to multiple internal holes, and the higher the density of holes, the more cracks there are around that area. These phenomena indicate that cracks tend to propagate along the path with the most severe stress concentration, and pores are definitely the main areas of stress concentration. Larger and denser pores intensify this effect, thereby reducing resistance to crack propagation.

To investigate the evolution and development of cracks in depth and reveal the relationship between pore size, porosity and crack development, the PFC2D software was used to depict the process of crack initiation, propagation and final failure of the specimen during uniaxial compression, as well as the displacement distribution of various internal points. Fig. 15(a) shows the failure process and displacement field of the model with a pore diameter of 2 mm and a porosity of 1.5%, Fig. 15(b) with a pore diameter of 3 mm and a porosity of 2.5%, and Fig. 15(c) with a pore diameter of 2 mm and a porosity of 2.5%.

As shown in Fig. 15(a) (with a pore diameter of 2 mm and a porosity of 1.5%), when the simulation loading reaches the crack initiation point ①, microcracks begin to appear inside the specimen. The cracks, which are few in number, are located at the specimen edge, near the stressed end faces or around the internal pores. As the loading continues, a directional path starts to form at the upper right end of the specimen at point ②, which means the cracks mainly develop toward the upper right direction, with the displacement field showing a uniform layered distribution. When the specimen is loaded at points ③ and ④, the microcracks develop rapidly,

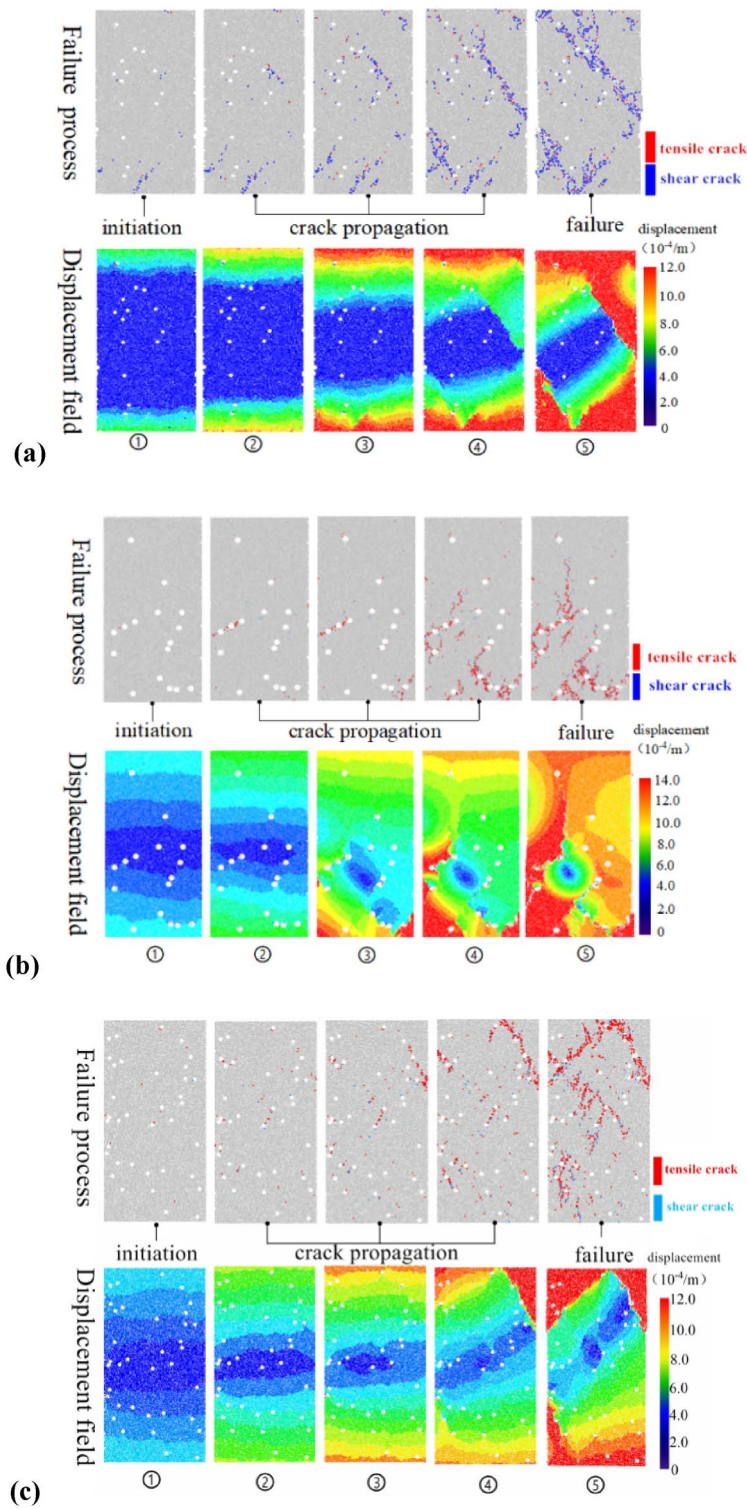


Fig. 15. (a) The failure process and displacement field of the specimen with a pole diameter of 2 mm and a porosity of 1.5%. (b) The failure process and displacement field in specimen with a pole diameter of 3 mm and a porosity of 2.5%. (c) The failure process and displacement field in specimen with a pole diameter of 2 mm and a porosity of 2.5%.

expanding with internal pores as nodes and connecting to adjacent pores. Moreover, partial crack penetration causes sudden displacement changes. Finally, the specimen exhibits obvious shear splitting failure at point ⑤, indicating that the failure under this parameter is dominated by shear cracks.

In Fig. 15(b) (with a pore diameter of 3 mm and a porosity of 2.5%) and Fig. 15(c) (with a pore diameter of 2 mm and a porosity of 2.5%), the failure of the specimens is dominated by tensile cracks. Comparative analysis of Fig. 15(a) and Fig. 15(c) (with the pore diameter fixed at 2 mm and porosity varied) reveals that the initiation positions of microcracks are more dispersed in Fig. 15(c). Besides the stressed end faces of specimens, the feature of synchronous multi-point initiation appears around the internal pores. Moreover, tensile cracks appear earlier than shear cracks, and the displacement field changes from a uniform layered distribution to “differential displacement between pores”. This phenomenon indicates that porosity is a key parameter regulating the dominant type of cracks and the macroscopic failure mode—specifically, shear stress transfer dominates under low porosity (1.5%), while tensile stress concentration zones are prone to form under high porosity (2.5%). Further comparison between Fig. 15(b) and Fig. 15(c) (with the porosity fixed at 2.5% and pore diameter varied) shows that the specimen deformation with a pore diameter of 3 mm is significantly greater than that with a pore diameter of 2 mm. This is because an increase in pore diameter raises the stress concentration coefficient around pores, which accelerates the propagation of tensile cracks and intensifies the relative displacement between particles, eventually leading to an increase in the overall deformation of the specimens.

To quantitatively verify the differences in the dominant crack types in Fig. 15 mentioned above, diagrams of the variation of crack number and failure location are plotted for the cases with a pore diameter of 2 mm (1.5% porosity) and a pore diameter of 2 mm (2.5% porosity), as shown in Fig. 16. When the pore diameter is 2 mm and porosity is 1.5%, shear microcracks first appear inside the specimen, with a maximum count of 716—far exceeding the number of tensile cracks (145). Therefore, the specimen exhibits shear failure due to the extensive penetration of shear cracks. In contrast, when the pore diameter is 2 mm and porosity is 2.5%, the opposite scenario occurs: tensile microcracks emerge earlier than shear microcracks, and the number of tensile cracks is much higher than that of shear cracks when the specimen fails. This indicates that both tensile stress and shear stress play roles in the failure process of specimens. This further confirms that the specimen failure is dominated by shear stress transfer under low porosity (1.5%), while the specimen failure mode is tensile failure under high porosity (2.5%)—ultimately leading to significant differences in crack development states and failure modes between the two sets of pore parameters.

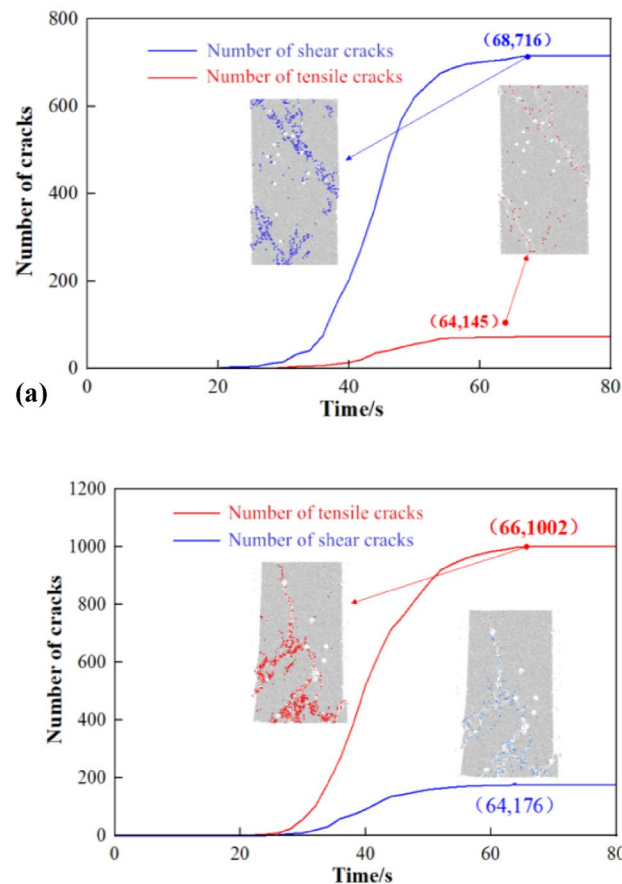


Fig. 16. (a) Number and position of cracks with a pole diameter of 2 mm and a porosity of 1.5% (b) Number and position of cracks with a pole diameter of 3 mm and a porosity of 2.5%.

Parameter type	Laboratory test	Numerical simulation	Comparison
Boundary condition	Displacement-controlled loading with steel rigid platens	Displacement-controlled loading with rigid walls at the top and bottom of the mode	Both are rigid displacement boundaries
Loading rate	0.02 mm/s (quasi-static)	0.02 mm/s (quasi-static)	Both are quasi-static displacement loading
Peak stress	23.8MPa	26.1MPa	a relative error of approximately 9.4%
Peak strain	6.8×10^{-3}	6.3×10^{-3}	a relative error of approximately 7.4%
Elastic modulus	3.5GPa	4.1GPa	a relative error of approximately 17.1%

Table 6. Correspondence parameters between numerical simulation and laboratory test.

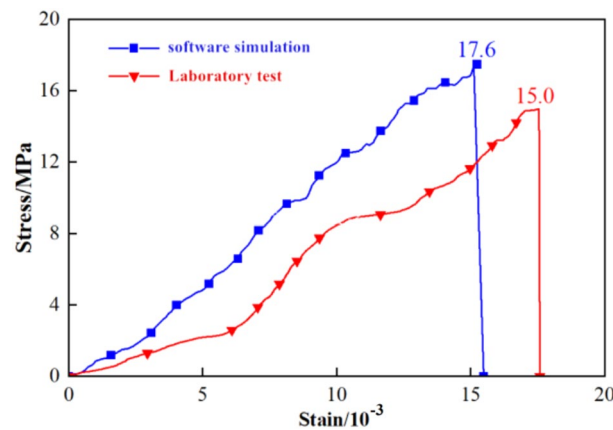


Fig. 17. The stress-strain curves of numerical simulation and laboratory test.

The analysis of stress-strain curve

To verify the rationality of the numerical simulation results, Table 6 compares the boundary conditions, loading rate, and mechanical parameters (including peak stress, peak strain, and elastic modulus) between the laboratory tests and the numerical simulation. This comparison reflects the degree of agreement between the simulation results and the experimental results. Moreover, Fig. 17 presents the comparison between the stress-strain curves of specimens without pores obtained from laboratory tests and numerical simulations, which intuitively shows the overall trend and local deviations of their mechanical responses, thereby providing support for the reliability of the simulation results.

As observed in Fig. 17, there exists a certain discrepancy between the stress-strain curves of the laboratory test and numerical simulation, namely the stress obtained from the numerical simulation is higher than that from the laboratory test under the same strain. After analysis, multiple factors contribute to the observed errors: First, the contact between spherical particles in the simulation is an ideal point contact, and stress transfer efficiency depends on the uniform distribution of contact stiffness and parallel bond strength. However, the angular interlocking effect of actual particles forms a multi-contact network, where local stress tends to disperse or concentrate due to surface undulations. Second, the failure of the parallel bond model follows the “strength criterion”, but microcrack initiation at the bond interface of actual cement-based materials may occur earlier than the theoretical strength. Consequently, the macroscopic mechanical response in laboratory tests enters the nonlinear stage earlier, and the stress growth rate is lower than that of the simulation curve. Third, due to the limitations of mesoscopic parameter calibration, the trial-and-error method may excessively enhance the contact stiffness parameters to match the peak indicators. This leads to an overall higher stress value of the simulation curve from the elastic stage to the pre-peak stage.

In summary, the errors essentially reflect the differences in mesoscopic mechanisms and parameter matching between laboratory tests and numerical simulations. Nevertheless, the consistency in curve trends indicates that the PFC2D model can effectively reproduce the macroscopic mechanical response characteristics of rock-like materials through reasonable calibration, providing a reliable numerical tool for subsequent studies on the mechanical behavior of specimens with pores.

To further investigate the influence of porosity on the stress-strain relationship, simulations were performed on specimens with identical pore diameters but varying porosities. This allowed for an analysis of stress variation under different porosity conditions. Fig. 18 illustrates the stress-strain curves of numerical simulation for specimens under different porosities (pore diameter 4 mm).

As shown in Fig. 18, when the internal pore size of the specimens is the same, the higher the porosity, the smaller the axial stress and the larger the axial strain of the specimens. This pattern is consistent with the results of laboratory tests and highly aligns with conclusions from existing literature—such as “increased porosity weakens rock strength” proposed by WU Tianhua et al.¹⁸ and “pore presence reduces the bearing capacity of

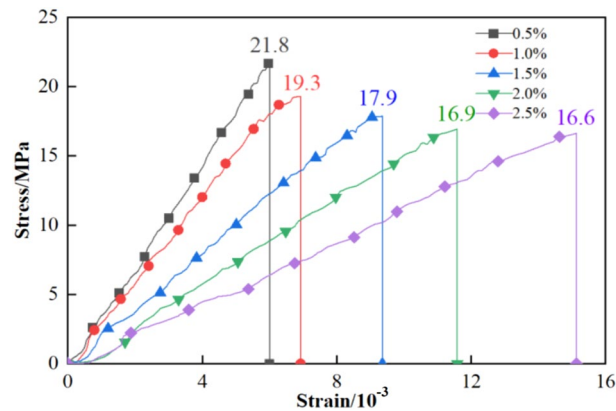


Fig. 18. The stress-strain curve of specimens under different porosities (pore diameter 4 mm).

rocks” identified by LIU Ping et al.²⁵. It further verifies the consistency of the law governing the influence of porosity on the mechanical properties of rock-like materials.

Moreover, compared to the experimental results, the simulated stress values at the same strain level are generally higher. This discrepancy can be attributed to the fact that artificially prepared specimens cannot achieve perfect homogeneity; they inherently contain minor defects, resulting in their quasi-homogeneous nature. These imperfections affect the propagation of stress waves. Additionally, heating during the test process may induce some degree of damage to the specimens, a factor not present in the numerical simulations. Therefore, the simulated specimens tend to exhibit superior mechanical performance compared to their physical counterparts. Despite these differences, the deviation remains within an acceptable range, confirming the overall reasonableness and validity of the simulation results.

Conclusions

Using the volume shrinkage characteristics of EPS particles after heating, researchers randomly created holes of different sizes in the rock-like specimens. Then, laboratory uniaxial compression tests were carried out, and the PFC2D software was used to simulate the failure process of specimens with prefabricated holes under uniaxial compression conditions. Finally, the effects of internal pore size and porosity on the mechanical properties, crack evolution, and failure characteristics of the specimens were analyzed, and the following conclusions were drawn:

- (1) The volume of EPS particles shrinks greatly at 200 °C, and the pore forming effect in specimens is remarkable. Moreover, the peak stress of specimens without pores still maintains good mechanical properties after heating, laying a foundation for the reliability of subsequent test results of specimens with pores.
- (2) When the pore diameters inside the specimens are the same, the peak stress of the specimens decreases with the increasing porosity, while the peak strain increases significantly. However, when the porosity is fixed, the peak stress of the specimens reduces generally with the rising pore size, while the peak strain increases. Moreover, under the combined conditions of large pore diameter and high porosity, the specimen exhibits an obvious strain mutation phenomenon during uniaxial compression. This can provide experimental reference for the early warning of sudden instability in natural defect-containing rocks.
- (3) PFC2D numerical simulation shows that the generation and development of internal cracks in specimens are related closely to the pore diameter and porosity. The larger and denser the holes are, the lower the load-bearing capacity is, and the failure process is the tension-shear composite mode rather than the single tensile failure. This phenomenon indicates that in the pore-dense area of underground engineering, it is necessary to strengthen the dual support strength combining shear resistance and tensile resistance.
- (4) Although minor discrepancies exist between the stress-strain curves obtained from indoor tests and numerical simulations, their overall trends are largely consistent. This agreement confirms that the PFC2D model demonstrates a reasonable level of reliability in predicting the mechanical behavior and failure modes of rock-like specimens containing internal pores.

Data availability

The data used to support the findings of this study are included within the article.

Received: 7 September 2025; Accepted: 30 October 2025

Published online: 28 November 2025

References

1. Jing, L. I. et al. Study on the influence of reservoir rock micro-pore structure on rock mechanical properties and crack propagation. *Rock Soil Mech.* **40**(11), 4149–4156+4164 (2019).
2. Xuewei, L. et al. Experimental study of effects of fracture type on strength characteristics and failure modes of fractured rockmass. *Rock Soil Mech.* **36**(S2), 208–214 (2015).

3. Fuqiang, R. et al. Dynamic response mechanism of rock-like materials with different shape holes. *Rock Soil Mech.* **45**(S1), 654–664 (2024).
4. Junhua, Z. H. O. U. et al. Effect of fissure on mechanical and damage evolution characteristics of sandstone containing hole defect. *J. Cent. S. Univ. (Sci. Technol.)* **50**(04), 968–975 (2019).
5. Henghua, L. et al. Fracturing and fractal evolution of rock mass containing hole-multiple fissures combined flaws. *Chin. J. Undergr. Sp. Eng.* **17**(04), 1021–1027 (2021).
6. Chuang, Z. et al. Experimental study of influences of pore number and pore size on mechanical properties of marble. *Rock Soil Mech.* **38**(S2), 41–50 (2017).
7. Yaoguang, H., Yangyang, L. I. & Wanxia, Y. Experimental study on tensile strength and splitting failure characteristic of rocks-like with eccentric cracks. *J. Min. Saf. Eng.* **41**(04), 824–835 (2024).
8. Diyuan, L. I. et al. Dynamic compressive mechanical properties of bedding sandstone with pre-existing hole. *J. Chin. Coal Soc.* **44**(05), 1349–1358 (2019).
9. Shusheng, W. A. N. G. et al. Research on phase-field simulation method of crack propagation of rock with pre-existing fissure. *Chin. J. Rock Mech. Eng.* **42**(02), 365–377 (2023).
10. Xuxu, Z. et al. Fracture test and analysis of rock-mass model with prefabricated defects. *Gold Sci. Technol.* **28**(02), 255–263 (2020).
11. Weijian, Y. U. & Mingjuan, Z. H. O. U. Rock mechanics characteristics and failure modes under different number of secondary fractures. *J. Min. Saf. Eng.* **42**(2), 394–403 (2025).
12. Bing, D. A. I. et al. Analysis on damage characteristics and energy dissipation of rock with a single hole under cyclic impact loads. *China Saf. Sci. J.* **30**(07), 69–77 (2020).
13. Yanbing, W. et al. Mechanical properties of sandstone with holes under impact load. *J. Min. Strata Control Eng.* **5**(01), 78–88 (2023).
14. Xiangjun, P. E. I. et al. Experimental study on acoustic emission characteristic of rocks with vein mass. *Chin. J. Rock Mech. Eng.* **39**(S1), 2602–2611 (2020).
15. Lei, Z., Xiaojing, X.U., Wangliang, X.U. et al. Acoustic emission response characteristics and early warning of prefabricated hole tuff failure. *J. Civil. Environ. Eng.* 1–11 (2024).
16. Yu, Z. et al. Particle flow analysis of acoustic emission characteristics during rock failure process. *Chin. J. Rock Mech. Eng.* **32**(05), 951–959 (2013).
17. Yu, W. et al. Investigation on fracture evolution of pre-flawed hollow-cylinder granite under increasing-amplitude cyclic loads. *Chin. J. Rock Mech. Eng.* **41**(7), 1325–1337 (2022).
18. Tianhua, W. U. et al. Mesoscopic study of interaction mechanism between circular hole and fissures in rock under uniaxial compression. *Rock Soil Mech.* **39**(S2), 463–472 (2018).
19. Guoyan, Z. H. A. O. et al. Micro-fracture evolution rule of sandstone specimens with a single hole under uniaxial compression. *J. Cent. S. Univ. (Sci. Technol.)* **50**(08), 1891–1900 (2019).
20. Bin, M. A. et al. Numerical simulation of uniaxial compression of heterogeneous rock based on fracture crack inclination angle. *J. Chongqing Jiaotong Uni. (Nat. Sci.)* **43**(10), 39–46 (2024).
21. Yangyang, L. I. et al. Study on mechanical properties and failure characteristics of cross-layer fracture composite rock with different dip angles. *J. Shandong. Univ. Sci. Technol. (Nat. Sci.)* **44**(1), 18–27 (2025).
22. Zhengyi, L. I. et al. Study on true triaxial mechanical characteristics with hole defects of sandstone. *Chin. J. Undergr. Sp. Eng.* **18**(01), 120–128 (2022).
23. Baoliang, Z. et al. Experimental study on fracture propagation law of precast rock mass of combined rock mass. *Chin. J. Rock Mech. Eng.* **43**(S2), 3690–3699 (2024).
24. Yujie, S. et al. Fracture mechanism of coplanar double-fracture composite rock under triaxial compression condition. *J. Vib. Shock.* **43**(21), 263–276 (2024).
25. Ping, L. I. U. et al. Effect of hole shapes on mechanical behavior of layered rocks using FDEM numerical method. *J. Cent. S. Univ. (Sci. Technol.)* **55**(02), 595–606 (2024).
26. Xingyu, F. et al. Numerical simulation of single-joint rock fracture evolution based on PFC. *J. Tsinghua Univ. (Sci. Technol.)* **64**(07), 1238–1251 (2024).
27. Xueping, Z. et al. Simulation research on granite compression test based on particle discrete element model. *Rock Soil Mech.* **35**(S1), 99–105 (2014).
28. Chongjin, L. I., Xibing, L. I. & Diyuan, L. I. Particle flow analysis of fracture characteristics of marble with a single hole. *Chin. J. Eng.* **39**(12), 1791–1801 (2017).
29. Jielong, S. et al. Mechanical properties test and PFC2D simulation of saturated fractured red sandstone under uniaxial compression. *J. Yan'an Univ. (Nat. Sci. Edit.)* **43**(4), 114–121 (2024).

Acknowledgments

Sincere gratitude goes to Professor XIONG Zu-qiang and Professor WANG Chun for his insights on research logic and data interpretation. Meanwhile, I appreciate Mr JI Xue-long for providing technical assistance in experimental operations, ensuring the reliability of the data.

Author contributions

CHENG Lu-ping : Writing-review & editing, Writing-original draft, Validation, Methodology, Data curation, Conceptualization. **XIONG Zu-qiang** : Data curation, Writing-original draft, Validation, Methodology. **JI Xue-long** : Writing-original draft, Validation, Methodology, Writing-review & editing, Methodology. **WANG Chun** : Data curation, Writing-original draft, Funding acquisition.

Funding

This research was funded by National Natural Science Foundation of China (52274076) and Henan Provincial Outstanding Youth Science Foundation (242300421070).

Declarations

Conflict of interest

The authors declare no competing interests.

Additional information

Correspondence and requests for materials should be addressed to W.C.

Reprints and permissions information is available at www.nature.com/reprints.

Publisher's note Springer Nature remains neutral with regard to jurisdictional claims in published maps and institutional affiliations.

Open Access This article is licensed under a Creative Commons Attribution-NonCommercial-NoDerivatives 4.0 International License, which permits any non-commercial use, sharing, distribution and reproduction in any medium or format, as long as you give appropriate credit to the original author(s) and the source, provide a link to the Creative Commons licence, and indicate if you modified the licensed material. You do not have permission under this licence to share adapted material derived from this article or parts of it. The images or other third party material in this article are included in the article's Creative Commons licence, unless indicated otherwise in a credit line to the material. If material is not included in the article's Creative Commons licence and your intended use is not permitted by statutory regulation or exceeds the permitted use, you will need to obtain permission directly from the copyright holder. To view a copy of this licence, visit <http://creativecommons.org/licenses/by-nc-nd/4.0/>.

© The Author(s) 2025